An improved numerical model of a UV-PCO reactor for air purification applications

Hao Luo[1], Guangxin Zhang[2], Zaher Hashisho[3], Lexuan Zhong[1] (✉)

1. Department of Mechanical Engineering, University of Alberta, Edmonton, AB, T6G 1H9, Canada
2. School of Materials Science and Engineering, Shandong University of Science and Technology, Qingdao 266590, China
3. Department of Civil and Environmental Engineering, University of Alberta, Edmonton, AB, T6G 2W2, Canada

Abstract

Ultraviolet photocatalytic oxidation (UV-PCO) is a promising gaseous volatile organic compounds (VOCs) elimination method, of which the PCO kinetics are closely related to the radiation and airflow (contaminants) fields. Mathematical models have been developed in extensive studies to demonstrate the PCO kinetic reactions. Computational fluid dynamics (CFD) simulation was also carried out to display the irradiance and flow fields in the reactor. However, it still lacks an in-depth understanding of the light and mass transfer within the porous film coating where the microscopic structures dominate. To close this gap, this paper concentrates on the development of mathematical models for describing the light propagation, mass transfer, and reaction kinetics within the porous film coating. Incorporated with a CFD model for solving the mass, momentum and energy conservation, the sophisticated PCO process in the reactor can be accurately reproduced. The developed models have been validated by the experimental data, and are comparable with other models in the literature. The developed numerical models provide the implications of mass transfer for film coating UV-PCO reactor design.

1 Introduction

Volatile organic compounds (VOCs) are one type of the most common indoor chemical contaminants with high vapor pressures. As a promising indoor gaseous VOC elimination method, photocatalytic oxidation (PCO) technology has gained increasing attention in the past decades. A UV-PCO reactor uses titanium dioxide (TiO_2) as a semiconductor as it generates electrons and positive holes upon the absorption of UV light. The subsequently formed hydroxyl radicals, as well as positive holes and superoxide radicals, act as oxidizing agents for the mineralization of organic molecules (Zhong and Haghighat 2011). Extensive experimental studies have been conducted on the UV-PCO reaction mechanisms: the direct attack by semiconductor holes, oxidation by hydroxyl radicals and reaction with superoxide radicals were reported as the three major degradation pathways (Bielski et al. 1985; Ishibashi et al. 2000; Murakami et al. 2007; Nosaka and

Nosaka 2017; Muñoz-Batista et al. 2019). And the UV-PCO reaction is inherently influenced by reactant concentration, humidity, temperature, flow rate, light intensity, etc., (Obee and Brown 1995; Yu et al. 2006, 2007; Chawengkijwanich and Hayata 2008).

A simulation study is another effective tool to investigate the complex UV-PCO system. The irradiance field in the reactor can be described by the preliminary mathematical models that treat lamps as radiation-emitting lines, surface source or volume source (Pareek et al. 2008). Further studies use the CFD modeling of radiation transport equation (RTE), which considers the varying conditions of the radiative properties, such as absorption, scattering and refractive indexes. Commonly used ones include the P-1 model (Cuevas et al. 2007), surface to surface model (S2S) (Einaga et al. 2015) and Discrete Ordinates (DO) model (Cuevas et al. 2007; Atkins and de Paula 2009; Denny et al. 2009; Trujillo et al. 2010; Duran et al. 2011). Among them, the DO radiation

E-mail: lexuan.zhong@ualberta.ca

List of symbols

a	geometric surface area per unit volume (m^{-1})		ρ	density (kg/m^3)
A_r	reaction area of the catalyst coating (m^2)		τ	tortuosity
c	solution concentration (mg/m^3)			
$[C]$	concentration (mg/m^3)		*Subscripts*	
d	mean particle diameter (m)		0	incident light
D	diffusivity (m^2/s)		1	electron capture
E	light flux (photons cm^{-2}·s^{-1})		2	hole capture
h	catalyst coating thickness (μm)		3	recombination
I	light intensity (W/m^2)		5	hydroxyl radical attack
k	rate constant (s^{-1})		7	radical termination
K	adsorption equilibrium constant (m^3/mg)		a	macropore
km	mass transfer coefficient (m/s)		ab	light absorption
l	light radiative properties (cm^{-1})		acetone	air property
L	length (m)		ads	absorbed surface equilibrium species concentration
M	intermediate (mg/m^2)		ai	mass transfer rate constant from macropore into mesopore
MS	molecular mass (g/mol)			
P	pressure (Pa)		b	bulk phase
q	absorbed concentration at the surface of the nanoparticle (mg/m^3)		BL	boundary layer
			c	coating
Q	volumetric flow rate (m^3/s)		ei	photocatalyst activation
r	reaction rate (mg/(m^2·s))		i	mesopore
$[R]$	acetone concentration (mg/m^3)		I	downward light
t	time (s)		in	inlet
T	temperature (K)		J	upward light
U	velocity (m/s)		kn	knudsen diffusion
x	distance (m)		M	molecular diffusion
z	depth (μm)		mfp	mean free path
α	constant		o	equilibrium concentration
β	constant		p	particle
δ	molecular collision diameter (nm)		rec	reaction
ε	porosity		s	solid-phase absorbed voc saturation capacity
η	light attenuation coefficient (m^{-1})		sc	light scattering
λ	light wavelength (nm)		t	time
μ	dynamic viscosity (kg/(m·s))		VOC	volatile organic compounds
ν	kinematic viscosity (m/s)		W	water

model is recognized with the capability of solving an entire range of optical thickness and solution at semi-transparent walls for giving the most accurate results. Also, the Do model was validated and employed in different kinds of reactor designs, such as slurry, flat plate, packed bed and immobilized reactors (Cuevas et al. 2007; Denny et al. 2009; Trujillo et al. 2010; Duran et al. 2011; Cheng et al. 2015). As for the fluid flow simulation, the CFD modeling of mass, momentum and energy conservation, as well as the multispecies transport equations, are solved to provide accurate fluid/thermal/ contaminant transport phenomena in a reactor (Taghipour and Mohseni 2005; Salvadó-Estivill et al. 2007b; Casado et al. 2017; Luo et al. 2019a; Malayeri et al. 2019). Furthermore, the irradiance and flow fields, which are difficult to be

determined by experiments, obtained from CFD simulation are critical input information for the PCO process in the catalyst coating.

With respect to the PCO process in the catalyst coating, photons transfer is normally neglected with the assumption of incident surface irradiance is the energy participating in PCO reactions. More realistic studies introduced the Beer-Lambert law with a non-scattering medium assumption $I = I_0 e^{-\eta z}$, which showed the exponential light decays with the catalyst depth z (Boyjoo et al. 2014). As for the mass transfer, preliminary studies proposed mass balance equations for the VOC transport in the bulk phase only (Salvadó-Estivill et al. 2007a; Jarandehei and de Visscher 2009; Wang et al. 2012; Adjimi et al. 2014). More comprehensive studies

included the advection and diffusion of the gas phase in the porous catalyst as well as the adsorption/reaction/desorption on the catalyst surface (Zhong and Haghighat 2011; Luo et al. 2019b). With respect to the PCO kinetic reaction, empirical Langmuir-Hinshelwood (L-H) reaction rate equation is extensively used to interpret the adsorption-reaction-desorption process with two lumped coefficients k and K as the reaction rate constant and adsorption coefficient, respectively (Murakami et al. 2003; Salvadó-Estivill et al. 2007b; Queffeulou et al. 2010; Zhong and Haghighat 2011; Zhong et al. 2013; Einaga et al. 2015; van Walsem et al. 2016). Several modifications were made to include the intrinsic influencing factors dependence, such as the light intensity, temperature, humidity, etc. (Wang et al. 1998; Li Puma et al. 2009; Zhong and Haghighat 2011; Zhu et al. 2015).

Despite that extensive simulation studies have been reported for UV-PCO performance, they do not correctly reflect the UV-PCO mechanism in the reactors. For example, the irradiance field within the porous catalyst was either simplified by a power-law empirical relationship (Salvadó-Estivill et al. 2007b) or Beer-Lambert law with the absence of scattering (Zhong and Haghighat 2011; Boyjoo et al. 2014). And the internal mass transfer resistance within the catalyst film was assumed negligible (Zhong and Haghighat 2011; Malayeri et al. 2019). Furthermore, the commonly used kinetic reaction rate equation from the L-H assumption cannot reveal the intrinsic reaction mechanism. Hence, in this paper, we developed new mathematical models in conjunction with the CFD model to investigate and simulate a plate UV-PCO reactor. The developed mathematical models described photon propagation, hierarchical mass transfer and quadratic adsorption-reaction-desorption reaction in the porous catalyst were validated by experimental data. The effects of operational conditions, such as VOC concentration, air flow rate and humidity, were explained by models.

2 Experimental setup of the UV-PCO system

The radiation measurements, dark adsorption tests and the

PCO reaction investigations were conducted in a UV-PCO reactor (Figure 1). The trapezoid PCO reactor (net volume = 130.19 cm^3) was gas-tight and consisted of a removable quartz-glass, a flat catalyst coating plate (103.83 mm × 83.31 mm), inlet and outlet nozzles and two baffles. The catalyst coating plate was supported by the baffles and located 5 mm lower than the bottom surface of the quartz-glass to create a narrow channel flow. The two baffles were located in front of the inlet and outlet nozzles (inner diameter = 6.35 mm, length = 15.3 mm) which stretched into the reactor at an angle of upward 15 degrees. Thus, the turbulent mixing of acetone and air was created when the inlet gas stream reached the baffle and then directed to flow through the catalyst plate. The coating area of 0.15g TiO$_2$/diatomite (properties see the Electronic Supplementary Material (ESM) Table S1 and Figure S1 in the online version of this paper) was 86.5 ± 2.6 cm^2. The reactor was irradiated by two UVA lamps (JINLI T5-8W, 0.0155 m blub diameter, 0.56 m blub length and 8 W UV-A output) side by side with the maximum irradiance peaks at 365 nm.

Our previous radiation measurements combined with the DO radiation model found the reflectance of pure aluminum plate and TiO$_2$/diatomite coating were 0.14 and 0.39, respectively, and the incident UV light I_0 at the catalyst surface was calculated as 13.133 W/m^2 (Luo et al. 2019b). In this work, acetone was selected as a challenge gas since it has been widely existing in an indoor environment (Salthammer et al. 2016; Zhang et al. 2016). The dynamic adsorption-PCO setup was used to determine the dark adsorption and PCO removal efficiency for the acetone under different operating conditions (Table 1 and the Electronic Supplementary Material Table S2). The system (see the Electronic Supplementary Material Figure S2) consisted a VOC generating syringe pump (Fusion 100, Chemyx Inc.), a humidity regulating system (bubble humidifier and mass flow controller (Alicat Scientific)) and VOC detecting system (analyzed with the total hydrocarbon (Series 9000, Baseline Mocon) and GC-FID (Agilent) for the inlet and outlet samples). Prior to UV light on, the reactor was continuously and steadily challenged with acetone to determine model
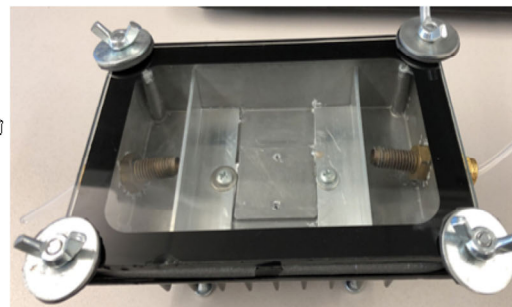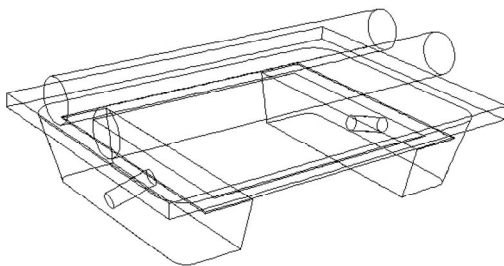

Fig. 1 Schematic diagram of the UV-PCO reactor

Table 1 Operation conditions of the UV-PCO reactor and corresponding mass transfer model parameters

No.	Inlet concentration (mg/m^3)	Volume flow rate (L/min)	Water concentration (mg/m^3)	External mass transfer coefficient km$_{BL}$ (m/s)	Mass transfer rate constant k_{ai} (s^{-1})	Equilibrium solid phase VOC concentration [R_{ads}] (mg/m^2)	Adsorption rate constant k_{ads} (s^{-1})
#1	23.99 ± 1.2		≈0 RH	0.0245		0.00269	0.040
#2	47.98 ± 2.4	1± 0.006	≈0 RH	0.0245		0.00321	0.099
#3	71.97 ± 3.6		≈0 RH	0.0245		0.00323	0.164
#4	95.96 ± 4.8		≈0 RH	0.0245		0.00361	0.182
#5		1 ± 0.006	≈0 RH	0.0245		0.00269	0.040
#6	23.99 ± 1.2	2 ± 0.012	≈0 RH	0.0344	14550	0.00173	0.065
#7		3 ± 0.018	≈0 RH	0.0427		0.00112	0.087
#8		4 ± 0.024	≈0 RH	0.0487		0.00054	0.163
#9			3450 (15% ± 2%RH)	0.0245		0.00048	0.422
#10	23.99 ± 1.2	1 ± 0.006	6900 (30% ± 2%RH)	0.0245		0.00032	0.914
#11			11500 (50% ± 2%RH)	0.0245		0.00028	1.302
#12			16110 (70% ± 2%RH)	0.0245		0.00019	5.064

parameters, such as external and internal mass transfer rate, adsorption isotherms, etc., from mass balance equations. Once the catalyst reached saturated adsorption, the UVA-lamps were switched on, and the PCO removal performance was evaluated by continuously measuring the inlet and outlet VOC concentrations for a stable period of 20-30 min.

3   Numerical models

3.1   CFD model governing equations

The fluid flow field was solved by the steady-state conservation equations with the shear-stress transport (SST) k-ω model, species transport equation and DO radiation model. The governing equations and constitutive equations are tabulated in Table 2.

3.2   UV-PCO model

3.2.1   Light propagation model

The Kubelka-Munk model was used to describe the radiative transfer in porous media with consideration of light absorption and scattering effects (Ciani et al. 2005). The light flux at a depth z was solved as (Ciani et al. 2005; Džimbeg-Malčić et al. 2012):

$$E_{\text{total}}(\lambda,z) = E_{\text{I}}(\lambda,z) + E_{\text{J}}(\lambda,z) = 2E_0\left(\phi_1 e^{\alpha z} + \phi_2 e^{-\alpha z}\right) \quad (1)$$

with

$$\phi_1 = \frac{(\beta-1)e^{-\alpha h}}{(1+\beta)^2 e^{\alpha h} - (1-\beta)^2 e^{-\alpha h}} \quad (2)$$

Table 2 Governing equations and constitutive equations

Conservation of mass	$\dfrac{\partial \rho}{\partial t} + \nabla \cdot (\rho \vec{v}) = 0$	
Conservation of momentum	$\dfrac{\partial (\rho v)}{\partial t} + \nabla \cdot (\rho v \vec{v}) = -\nabla P + \nabla \cdot \left(\overline{\overline{\tau}}\right) + \rho g$	ANSYS 2018
Conservation of species Y_i	$\dfrac{\partial (\rho Y_i)}{\partial t} + \nabla \cdot (\rho \vec{v} Y_i) = -\nabla \cdot \vec{J}_i + R_i$	
SST k-ω turbulence model	$\dfrac{\partial}{\partial t}(\rho k) + \dfrac{\partial}{\partial x_i}(\rho k u_i) = \dfrac{\partial}{\partial x_j}\left(\Gamma_k \dfrac{\partial k}{\partial x_j}\right) + \widetilde{G}_k - Y_k + S_k$ $\dfrac{\partial}{\partial t}(\rho \omega) + \dfrac{\partial}{\partial x_i}(\rho \omega u_i) = \dfrac{\partial}{\partial x_j}\left(\Gamma_\omega \dfrac{\partial \omega}{\partial x_j}\right) + G_\omega - Y_\omega + S_\omega + D_\omega$	Menter et al. 2003; ANSYS 2018
DO radiation model	$\nabla \cdot (I(\vec{r},\vec{s})\vec{s}) + (a+\sigma_s)I(\vec{r},\vec{s}) = an^2 \dfrac{\sigma T^4}{\pi} + \dfrac{\sigma_s}{4\pi}\int_0^{4\pi} I(\vec{r},\vec{s}')\Phi(\vec{s}\cdot\vec{s}')\mathrm{d}\Omega'$	ANSYS 2018

$$\phi_2 = \frac{(\beta+1)e^{\alpha h}}{(1+\beta)^2 e^{\alpha h} - (1-\beta)^2 e^{-\alpha h}} \tag{3}$$

where $\alpha = \sqrt{l_{ab}(l_{ab}+2l_{sc})}$, $\beta = \sqrt{l_{ab}/(l_{ab}+2l_{sc})}$, l_{ab} (cm^{-1}) and l_{sc} (cm^{-1}) are the light absorption and scattering coefficients, and $E_0(\lambda)$ (photons cm^{-2} s^{-1}) is the incident light flux at the top surface.

3.2.2 Mass balance equations

As presented in Figure 2, the catalyst coating is characterized as a film-bidisperse porous structure which is controlled by the following three-step mass transfer:
(1) The adsorbates transport in the bulk fluid flow and diffuse into the concentration boundary layer on the top of the catalyst coating.
(2) The adsorbates transport in the macropores (interparticle diffusion) of the catalyst coating and then are adsorbed on the macropore walls (external nanoparticle surface).
(3) The adsorbates transport in the mesopores (intraparticle diffusion) of nanoparticles and then are adsorbed on the mesopore walls.

Thus, the mass balance equations are established as:

i. Mass balance within the boundary layer:

$$\frac{\partial[C_b]}{\partial t} + U_0 \frac{\partial[C_b]}{\partial x} = D_{acetone}\frac{\partial^2[C_b]}{\partial x^2} - km_{BL}a_{BL}([C_b]-[C_a]) \tag{4}$$

ii. Mass balance within macro-porous catalyst coating:

$$\varepsilon_a \frac{\partial[C_a]}{\partial t} + (1-\varepsilon_a)a_a\frac{\partial[R_{aads}]_t}{\partial t} = \varepsilon_a \frac{\partial}{\partial x}\left[D_a\frac{\partial[C_a]}{\partial x}\right]$$
$$+ km_{BL}a_{BL}([C_b]-[C_a]) - k_{ai}([C_a]-[C_i]) \tag{5}$$

iii. Mass balance within mesoporous catalyst particle:

$$\varepsilon_i(1-\varepsilon_a)\frac{\partial[C_i]}{\partial t} + (1-\varepsilon_i)(1-\varepsilon_a)a_i\frac{\partial[R_{iads}]_t}{\partial t}$$
$$= \varepsilon_i(1-\varepsilon_a)\frac{\partial}{\partial x}\left[D_i\frac{\partial[C_i]}{\partial x}\right] + k_{ai}([C_a]-[C_i]) \tag{6}$$

iv. Adsorption at external nanoparticle surface and intraparticle adsorption:

$$\frac{\partial[R_{ads}]_t}{\partial t} = \frac{\partial[R_{aads}]_t}{\partial t} + \frac{\partial[R_{iads}]_t}{\partial t} - r_a - r_i$$
$$= k_{ads}([R_{aads}]+[R_{iads}]-[R_{ads}]_t) - r_a - r_i \tag{7}$$

v. UV-PCO reaction at nanoparticle external surface and intraparticle walls, considering oxidation by hydroxyl radicals is the dominant reaction pathway (Muñoz-Batista et al. 2019):

$$r = -\frac{\omega_1[R_{ads}][H_2O]}{(1+\omega_2[R]+K_W[H_2O])}\left(-1 + \sqrt{1+\frac{\omega_3 I(1+K_{VOC}[R]+K_W[H_2O])}{[H_2O]}}\right) \tag{8}$$

where

$$\omega_1 = \frac{k_5 k_1 k_2 K_W[R_s][O_{2ads}]}{2k_3 k_7[M]} \tag{9}$$

$$\omega_2 = \frac{(k_5 K_{VOC}[R_s]+k_7 K_{VOC}[M])}{k_7[M]} \tag{10}$$

$$\omega_3 = \frac{4k_{ei}k_3[sites_{TiO_2}]}{k_1 k_2 K_W[O_{2ads}][R_s]} \tag{11}$$
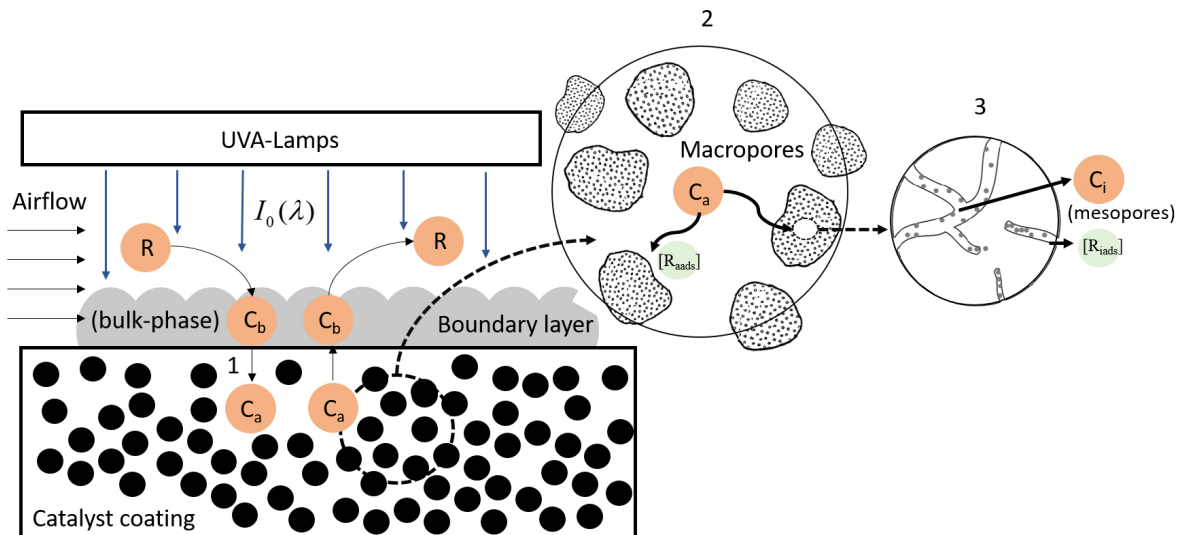
With the initial and boundary conditions are

Fig. 2 Schematic diagram of the VOC transfer in the catalyst coating

At $t = 0$, $C_b = C_a = C_i = [R_{iads}]_t = 0$ at any x (12)

At $x = 0$, $C_b = C_{in}$ and $\dfrac{\partial C_b}{\partial x} = \dfrac{\partial C_i}{\partial x} = 0$ at any t (13)

where a is the area available for external film mass transfer per unit volume (m²/m³); km_{BL} is the boundary layer mass transfer coefficient (m/s); ε_a and ε_i are the macroporosity and mesoporosity, respectively; $[R]$ is the gaseous VOC concentration (mg/m³); $[R_{ads}]_t$ is the absorbed VOC concentration (mg/m²); k_{ai} is the mass transfer rate from macropore to mesopore (s⁻¹); k_{ads} is the rate constant of particle adsorption (s⁻¹); D_a and D_i are the diffusivities in macro- and mesopores (m²/s), respectively; and $[H_2O]$ is the water vapor concentration (mg/m³). Equation (8) is a function of $[R_{ads}]$, $[H_2O]$ and I, where coefficients ω_1 (m³/(mg·s)), ω_2 (m³/mg) and $\omega_3 \left(\dfrac{m^2}{W} \cdot \dfrac{mg}{m^3} \right)$ are independent of physical parameters of interest. By varying the VOC compound concentration and RH conditions, the equation coefficients can be obtained.

4 Numerical methodology

The complex UV-PCO reaction simulations involve an accurate description of the flow field, radiation field, mass transfer and PCO reaction. This paper used Ansys Fluent 19.0 to simulate the macroscopic flow field and irradiance field in the reactor, which passed the boundary conditions to COMOSOL Multiphysics 5.4 to study the microscopic mass transfer in the porous catalyst. The obtained reaction rate was implemented back to the Fluent through user-defined function (UDF), and the flow field after the UV-PCO reaction was solved. Furthermore, the light distribution along catalyst coating depth was solved in MATLAB R2018b and the average absorbed light flux was implemented into the kinetic reaction model.

Accurate simulations require high-quality meshes. In this work, the 3D model was constructed for the reactor (mesh sees the Electronic Supplementary Figure S3). The boundary of the top domain of the reactor was not shown for visibility. The tetrahedron mesh was built here due to the complex reactor geometry, while the refinement in the catalyst region was built to increase the numerical accuracy of the domain of interest, which contains three layers elements with 1.1 height increasing ratio up to 0.5 mm maximum layer size. The mesh independence was examined under three different global element seed size (4.0 mm, 2.0 mm, and 1.0 mm). The grid convergence index (GCI) was tested for the average velocity at plane 1 and the average incident radiation at plane cata (see the Electronic Supplementary Material Figure S4). The calculated GCIs with safety factor (Fs=1.25) were within 5%, and the refinement was in the asymptotic range of convergence (≈1).

Thus, the grid convergence was reached and the medium mesh 2.0 mm was adopted to reduce the calculation time while ensuring accurate results.

The lamp was considered as a semi-transport wall with 15 W/m² emitting diffuse radiation, which was measured by applying a radiometer (UVP model UVX-38) on the lamp surface. The inlet, outlet, and space were considered as a semi-transport wall with zero-emitting radiation such that the radiation transmits freely without reflection and refraction. Furthermore, the quartz-glass was defined as a semi-transparent wall with 99.5% transmittance, which was determined by the ratio of measured radiation intensity before and after applying the quartz-glass. Other walls were considered as opaque walls with prescribed absorption coefficients, including 0.8 for lamp base (Janecek 2012), 0.9 for detector (Ishii and Ogawa 2004), 0.9 for detector probe (Janecek 2012), 0.8 for reactor wall (MATERION n.d.), 0.86 and 0.61 for catalyst coating and pure plate (Luo et al. 2019b). With respect to the flow field boundary conditions, mixed air with varying acetone contributions, water vapors, and flow rates was introduced. The outlet was set as outflow, and all other walls were set as stationary walls with no-slip boundary conditions. As for the operating conditions, the radiative properties of injected VOC were considered the same as the fresh lab air since the VOC concentration was very low. Therefore, the absorption coefficient, scattering coefficient, and refractive index of the airflow were defined as 0.000014 (Bucholtz 1995), 0.00006 (Bucholtz 1995) and 1.003001 (Penndorf 1957), respectively. All the boundary conditions used in the CFD software were tabulated in the Electronic Supplementary Material Table S4.

The finite volume method (FVM) was used to solve governing equations as well as the SST k-ω turbulence model and the DO radiation model (Table 2) in Fluent. The SIMPLE scheme was used for the pressure-velocity coupling. The second-order upwind scheme was chosen to discretize mass and momentum governing equations as well as convection terms for the k-ω turbulence model. Furthermore, the convergence criteria were set as 1×10^{-4}, 1×10^{-6} and 1×10^{-9} for flow field parameter, radiation intensity and species transport, respectively. The adsorption mass balance equations were solved in COMSOL Multiphysics using the finite element method (FEM). The Lagrange type shape function along with quadratic element discretization was used, and the convergence criteria were set as 1×10^{-4}.

5 Results and discussion

5.1 Determination of model parameters

5.1.1 Light penetration model

The radiation transport equations in air and quartz-glass

are solved by DO radiation model, of which the sensitivity analyses for the number of discrete solid angles and angular overlapping were conducted. Then the UV light reflectance of TiO$_2$/diatomite catalyst coating was determined by the methodology introduced in our previous paper (Luo et al. 2019b). The UV light reflectance of catalyst coating and plate were obtained as 0.14 and 0.39, respectively. Thus, the light being absorbed by the catalyst is calculated as 13.133 W/m^2.

The light transport within the porous media goes through nanoparticle absorption, scattering, reflection and substrate reflection (Figure 3). From the literature, the absorption coefficient and scattering coefficient of TiO$_2$ were adopted as 800 (cm^{-1}) and 302 (cm^{-1}), respectively (Elim et al. 2011; Shehap and Akil 2016; Shinen et al. 2018; Tobaldi et al. 2019). Implementing them into the Eq. (1), the light propagation with respect to the penetrating depth of catalyst coating is shown in Figure 4, indicating 10% of the original UV light flux at h = 21.8 μm. The catalyst coating of our experiment was 10 μm. Thus the light flux within 10 μm range of catalyst coating was averaged and converted to light intensity as 7.599 W/m^2 that maintained 57% of I_0.

5.1.2 Adsorption mechanisms

Concentration boundary layer
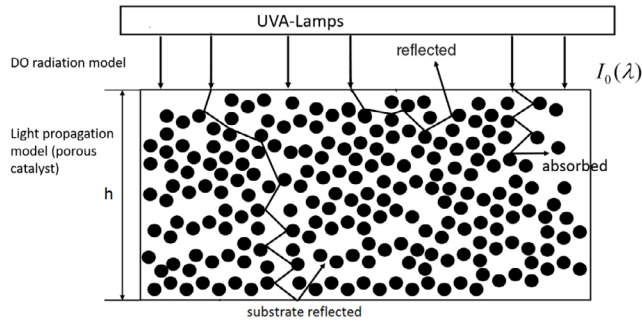
The mass transfer coefficient from the boundary layer into

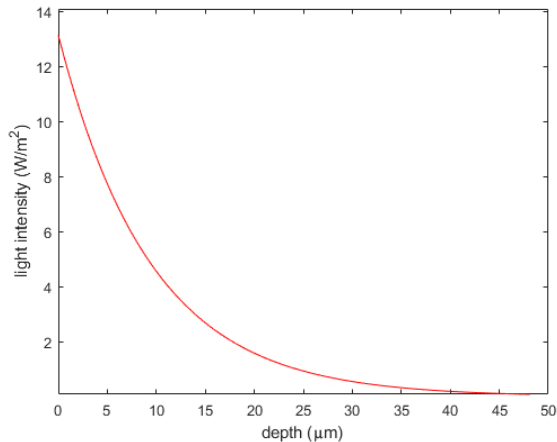**Fig. 3** Schematic diagram of photon transport in a porous media

Fig. 4 Predicted light transport inside the TiO$_2$ coating

the catalyst pore structure km$_{\mathrm{BL}}$ was determined by Sherwood number as follow (Cussler and Cussler 2012):

$$\mathrm{km}_{\mathrm{BL}x} = \frac{Sh_x D_{ij}}{L_c} = \frac{0.0296 \left(\frac{xU_0}{\nu}\right)^{\frac{4}{5}} \left(\frac{\nu}{D_{ij}}\right)^{\frac{1}{3}} D_{ij}}{L_c} \quad (14)$$

with $\quad \overline{\mathrm{km}_{\mathrm{BL}}} = \dfrac{1}{L_c} \displaystyle\int_0^{L_c} \mathrm{km}_{\mathrm{BL}x}\, \mathrm{d}x$

where D_{ij} is the mass diffusivity, L_c is the plate length, U_0 is the freestream velocity, ν is the kinematic viscosity. With the help of CFD, the flow field, the local Sherwood number, and the mass transfer coefficient were calculated to account for the boundary layer growth on the plate. The averaged mass transfer coefficients were tabulated in Table 1.

Mass transfer rate into TiO$_2$ nanoparticles

The mass transfer rate constant from macropores into the TiO$_2$ nanoparticles is given as (Kast 1985; Snyder 1992):

$$k_{\mathrm{ai}} = \Omega \frac{D_i}{r_p^2} \frac{c_o}{q_o} = \frac{60 D_i}{d_P^2} \quad (15)$$

where D_i is the intraparticle diffusion coefficient and d_p is the nanoparticle diameter. Considering the intraparticle mesopore with a size of 6 nm, the mean free path can be calculated with the following equation (Zhang 2013):

$$L_{\mathrm{mfp}} = \frac{k_B T}{\sqrt{2}\pi\delta^2 P} \quad (16)$$

where k_B is the Boltzmann constant, 1.38×10^{-23} J/K; P is the mean total pressure with the pores in adsorbent (Pa); δ is the molecular collision diameter for acetone, 0.616 nm; and T is the absolute temperature (K). Thus, the mean free path was calculated as 14 nm, which proved that the Knudsen diffusion effect existed in the mesoporous TiO$_2$ nanoparticles. The intraparticle diffusion coefficient can be estimated as:

$$D_i = \frac{\varepsilon}{\tau} \frac{1}{\left(\dfrac{1}{D_M} + \dfrac{1}{D_{kn}}\right)} \quad (17)$$

where $\quad D_{kn} = \dfrac{d_p}{3}\left(\dfrac{8RT}{\pi MS_i}\right)^{0.5}$

The estimated Knudsen diffusion coefficient and intraparticle diffusion coefficient were 6.59×10^{-7} m^2/s and 9.70×10^{-8} m^2/s, respectively.

Macropore and mesopore intraparticle adsorption

The model parameters k_{ads} and $[R_{\mathrm{ads}}]$ were determined from the adsorption kinetic experiments. The overall adsorption isotherm was described by a classical molecular single-site competitive Langmuir isotherm under different VOC

concentrations:

$$[R_{ads}] = \frac{[R_s]K_{VOC}[C]}{1 + K_{VOC}[C] + K_W[H_2O]} \tag{18}$$

which can be rearranged as:

$$\frac{1}{[R_{ads}]} = \frac{1 + K_W[H_2O]}{[R_s]K_{VOC}} \frac{1}{[C]} + \frac{1}{[R_s]} = \frac{K_W}{[R_s]K_{VOC}[C]}[H_2O]$$
$$+ \frac{1 + K_{VOC}[C]}{[R_s]K_{VOC}[C]} \tag{19}$$

where $[C]$ and $[H_2O]$ are the gas phase VOC and water concentration (mg/m³), respectively; $[R_s]$ and $[R_{ads}]$ are the catalyst absorbed VOC saturation capacity and equilibrium solid-phase VOC concentration (mg/m²), respectively; K_{VOC} and K_W are the adsorption equilibrium constant (m³/mg). The operating conditions #1-4 and #9-12 were implemented in Eq. (19) and the equilibrium adsorption isotherms were presented in Figure 5. The $[R_s]$, K_{VOC} and K_W were obtained as 0.00391, 0.0915 and 0.00266 m³/mg, respectively. Furthermore, with the assumption of the same adsorption properties for the external macropore surface and intraparticle mesopore surface, the fraction of adsorption saturation is proportional to the specific surface area. The analyzed TiO₂ external and internal surface areas were 0.104 m²/g and 39.896 m²/g, respectively. Thus $[R_{aads}]/[R_{iads}]=0.0026$, with the known $[R_{ads}]$, the equilibrium solid-phase concentration at external and internal nanoparticle surfaces can be obtained.
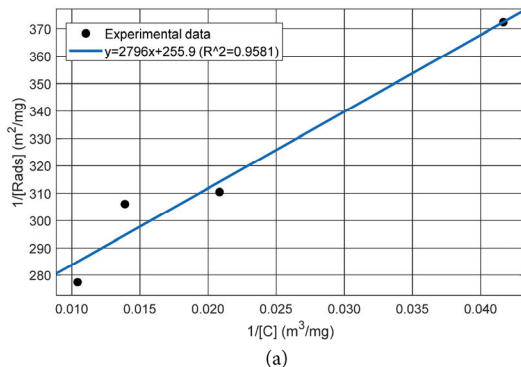
The adsorption rate constant, k_{ads}, was estimated by fitting the breakthrough curve on the time axis with the integral of Eq. (5), which has a form:

$$[R_{ads}]_t = [R_{ads}]\left(1 - e^{-k_{ads}t}\right) \tag{20}$$

The results were presented in Figure 6 and the adsorption rate constants were tabulated in Table 1.

5.1.3 Kinetic reaction model

The reaction rate was computed by the function:

$$r = -\frac{Q(C_{in} - C_{out})}{A_r} \tag{21}$$

where Q is the volumetric flow rate of the VOC carried air stream (m³/s); C_{in} and C_{out} are the averaged acetone concentrations of the inlet and outlet of the reactor (mg/m³), respectivley; and A_r is the reaction area of the catalyst coating (6 m²). The operating conditions #9-12 were used for data fitting. Equaiton (8) was simplified to Eq. (22) due to that acetone concentration was much lower than the water concentration:

$$r = -\frac{\beta_1[H_2O]}{(1 + K_W[H_2O])^2}\left(-1 + \sqrt{1 + \frac{\omega_3 I(1 + K_W[H_2O])}{[H_2O]}}\right) \tag{22}$$

where $\beta_1 = \omega_1 K_{VOC}[R_s][C]$. The data fitted Eq. (22) was obtained as

$$r = -\frac{5.14 \times 10^{-3}[H_2O]}{(1 + 2.66 \times 10^{-3}[H_2O])^2}\left(-1 + \sqrt{1 + \frac{1.71 \times 10^{-2} I(1 + 2.66 \times 10^{-3}[H_2O])}{[H_2O]}}\right)$$

and plotted in Figure 7. The fitting agreed with experimental data, and the reaction rate decreased with the increase of humidity levels, which was attributed to the competitive adsorption between VOC and water molecules.

With respect to the operating conditions #1-4 (significant low water concentration), Eq. (8) was simplified as:

$$r = -\frac{\omega_1[R_{ads}][H_2O]}{(1 + \omega_2[R])}\left(-1 + \sqrt{1 + \frac{\omega_3 I(1 + K_{VOC}[R])}{[H_2O]}}\right) \tag{23}$$

At a very low $[H_2O]$, $\omega_3 I/[H_2O]$ was large, and the bracket can be simplified as:

$$r = -\frac{\omega_1[R_{ads}]}{(1 + \omega_2[R])}\sqrt{\omega_3 I(1 + K_{VOC}[R])[H_2O]}$$
$$= \frac{\omega_1\sqrt{\beta_2(1 + K_{VOC}[R])}}{(1 + \omega_2[R])}[R_{ads}] \tag{24}$$
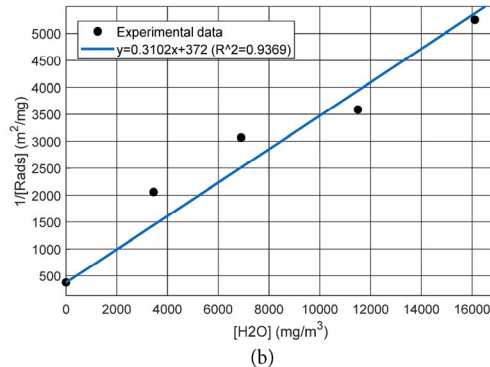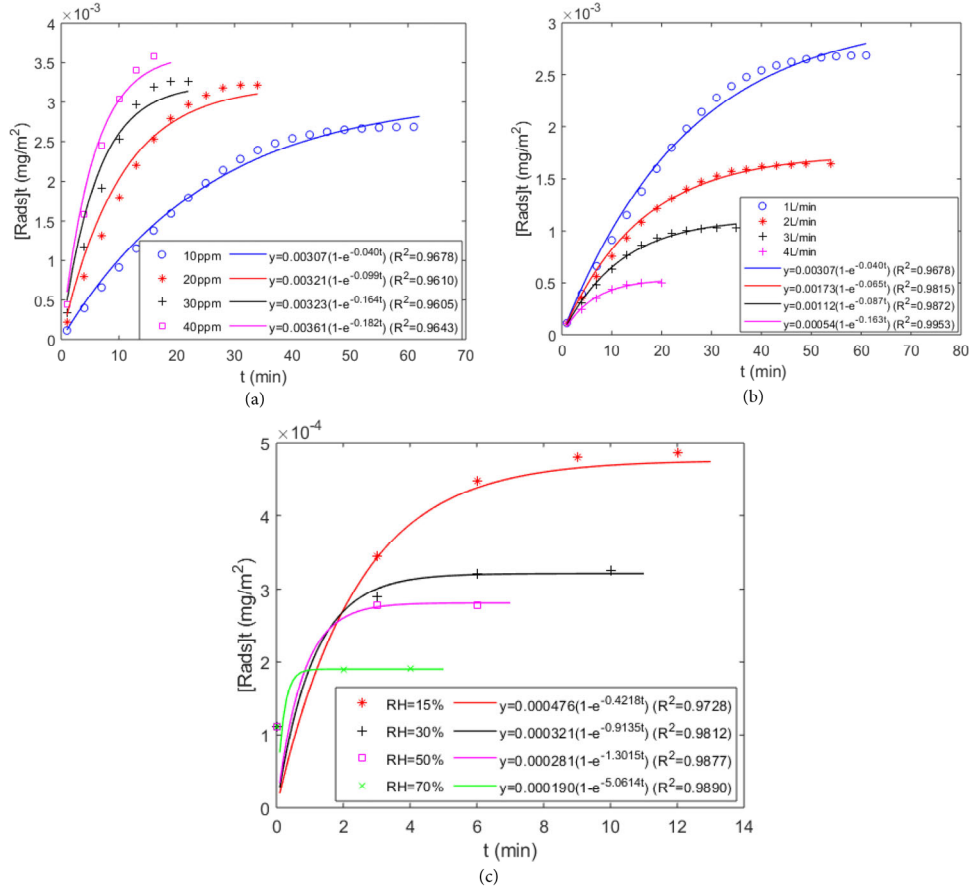

Fig. 5 Adsorption isotherms with respect to (a) different inlet VOC concentrations and (b) different RH
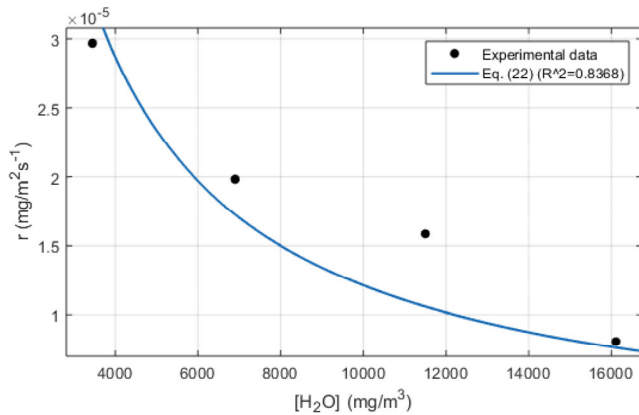
Fig. 6 The model fitted breakthrough curves for the adsorption of acetone under different (a) inlet concentrations, (b) volume flow rates and (c) humidity ratios

where $\beta_2 = \omega_3 I[H_2O]$. Replaced with fitted data, Eq. (24) was

changed to $r = -\dfrac{0.591\sqrt{0.9525\left(1 + 3.91 \times 10^{-3}[R]\right)}}{\left(1 + 2.7[R]\right)}[R_{ads}]$.

Figure 8 shows the experimental data of oxidation rates versus absorbed catalyst surface VOC concentrations. The dependence of the reaction rate on acetone concentration was well represented by the model.

With the known β_1, K_{VOC}, $[R_s]$ and $[C]$, ω_1 was calculated from the data fitting of Eq. (22) as 0.599, which showed a 1.34% difference with the ω_1 obtained from the data fitting of Eq. (24). Thus, the model parameters were consistent. Furthermore, with the known ω_3, I, and β_2, $[H_2O]$ for operating conditions #1-4 was solved as 7.3 mg/m³, confirming water vapor was very close to 0% RH.

Fig. 7 Data fitting of Eq. (22) for reaction rates under different water vapors
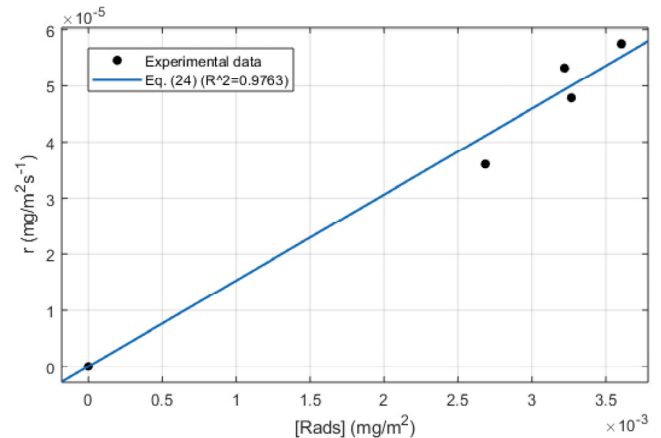
Fig. 8 Data fitting of Eq. (24) for reaction rates under different equilibrium solid phase VOC concentrations

5.2 Comparison of model results with experimental data

5.2.1 Dark adsorption

Transient mass balance equations were solved by COMOSOL Multiphysics with the determined model parameters. The model predictions of different operating conditions were plotted against experimental data and presented in Figure 9. The numerical predictions agree well with the experimental data. When increasing inlet VOC concentration (#1-4), the time reaching equilibrium was shorter, indicating faster mass transfer from the increased bulk and absorbed VOC concentration. The same conclusion was made from Table 1 as both the $[R_{ads}]$ and k_{ads} increased with inlet VOC concentration. On the other hand, increasing air flowrate (#5-8) shortened the time reaching equilibrium. The kinetic adsorption parameters in Table 1 confirms what we observed in the experiments as the km_{BL} and k_{ads} increased with the airflow rates. Increasing humidity (#9-12) significantly shortened the adsorption time and decreased the equilibrium solid phase VOC concentration. It is attributed to the competitive adsorption between water molecules and VOC molecules at the TiO_2 surface adsorption sites. And another reason is the adsorption forces between VOC and TiO_2

composite are weakened by the by the hydrogen bonds of water molecules with surface hydroxyls of composite within the water layers (Zhang et al. 2020).

5.2.2 Kinetic reaction

Kinetic reaction model Eq. (8) was implemented into mass balance equations for predicting the transient outlet VOC concentration under different operating conditions. $[R_{ads}]$ increased with the inlet VOC concentration, thus increasing the reaction rate (Figure 10 (a)). On the contrary, increasing the airflow rate shortened the residence time (contact time) between VOC molecules and catalyst coating, leading to the decrease of $[R_{ads}]$, and thus resulting in the decrease of reaction rate, even though the inlet VOC concentration maintains the same (Figure 10 (b)). Increasing humidity significantly suppressed the $[R_{ads}]$, decreased the reaction rate as indicated in Figure 9 and Eq. (8), and thus increased outlet VOC concentrations.

5.3 Comparison with other models in the literature

The obtained model parameters were compared with the literature data for validating the applicability. The
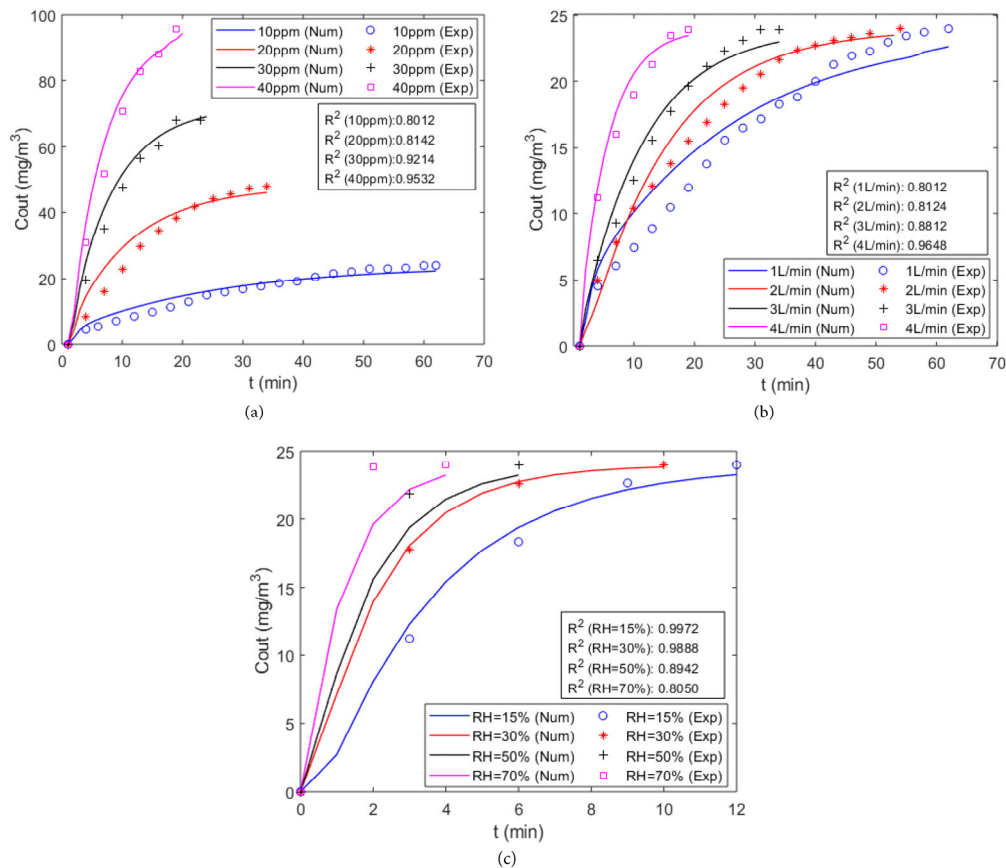
Fig. 9 Comparisons of model predictions and dark adsorption experiment data under different operating conditions of (a) VOC inlet concentration, (b) volume flow rates and (c) humidity ratios
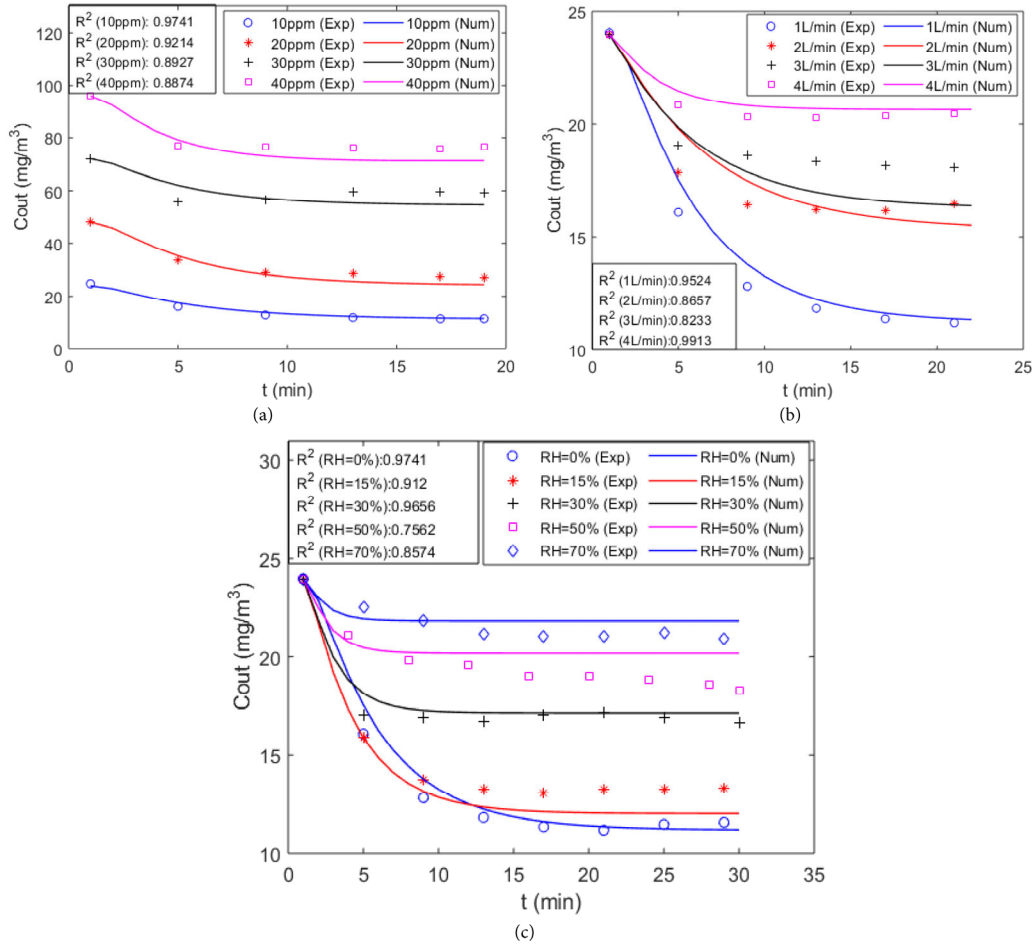
Fig. 10 Comparison of model predictions and UV-PCO reaction experiment data under different operating conditions of (a) VOC inlet concentrations, (b) volume flow rates and (c) humidity ratios

rearrangement of Eq. (8) was conducted to have a similar form comparable with the L-H kinetic reaction model:

$$r = -\frac{\omega_1[H_2O]\theta}{(1+\omega_2[R]+K_W[H_2O])}[R_{ads}] \equiv -\frac{k_{rec}K_{VOC}}{1+K_{VOC}C}C \quad (25)$$

where

$$\theta = \left(-1+\sqrt{1+\frac{\omega_3 I(1+K_{VOC}[R]+K_W[H_2O])}{[H_2O]}}\right) \quad (26)$$

The model parameters θ, $1+\omega_2[R]+K_W[H_2O]$ and $\omega_1[H_2O]$ had the units of 1, 1 and s^{-1}, respectively. Thus, the coefficient $\frac{\omega_1[H_2O]\theta}{(1+\omega_2[R]+K_W[H_2O])}$ (s^{-1}) is comparable with the $\frac{k_{rec}K_{VOC}}{1+K_{VOC}C}$ (s^{-1}) due to the similar physical meaning and the same unit. The comparison was presented in Table 3. Even though the derivations of the kinetic mechanism were different, the overall kinetic reaction/adsorption constants from this study were comparable with previous work. Thus,

the model in this work was well validated.

5.4 CFD modeling of the UV-PCO reactor

The resolved flow and irradiance fields by 3D CFD modeling of the reactor are shown in Figure 11. The VOC streamline distributions colored by the velocity as shown in Figure 11(a) are on the scale of 1:50. It is shown the well-mixed VOC and air was injected from nozzle inlet, spread out after reaching the baffles, deviously climbed over and flowed through the plate, and gathered at the outlet with outflow condition. The flow field was observed uniform above the catalyst plate. As shown in Figure 11 (b), there were small fluctuations which were attributed to the turbulence from the baffles. Furthermore, The flow was developed uniform (axial velocity distribution) along the flow direction as plotted in the Electronic Supplementary Material Figure S5. This observation supported the plug flow assumption for the reactor. Figures 11 (c) and (d) present the radiation distributions on the catalyst and lamp surfaces. It can be seen the accumulated radiation intensity at the central region

Table 3 Kinetic parameters of the quadratic type rate equation and L-H reaction rate equation

Acetone concentration (ppm)	RH (%)	Kinetic constant k_{rec} (mg/(m³·s))	Adsorption constant K_{VOC} (m³/mg)	$\dfrac{k_{rec}K_{ads}}{1+K_{ads}C}$ or $\dfrac{\omega_1[H_2O]\theta}{(1+\omega_2[R]+K_2[H_2O])}$ (s⁻¹)	Ref.
0.25–2	43.2	505.8	1.33×10^{-5}	6.75×10^{-3}	Zhong et al. 2013
37–450	≈ 0	2.13	6.75×10^{-3}	1.73×10^{-3} to 8.99×10^{-3}	Kim and Hong 2002
590	23	244.67	3.5×10^{-4}	5.73×10^{-2}	Alberici and Jardim 1997
10–40	≈ 0	—	9.15×10^{-2}	1.38×10^{-3} to 1.85×10^{-3}	This work
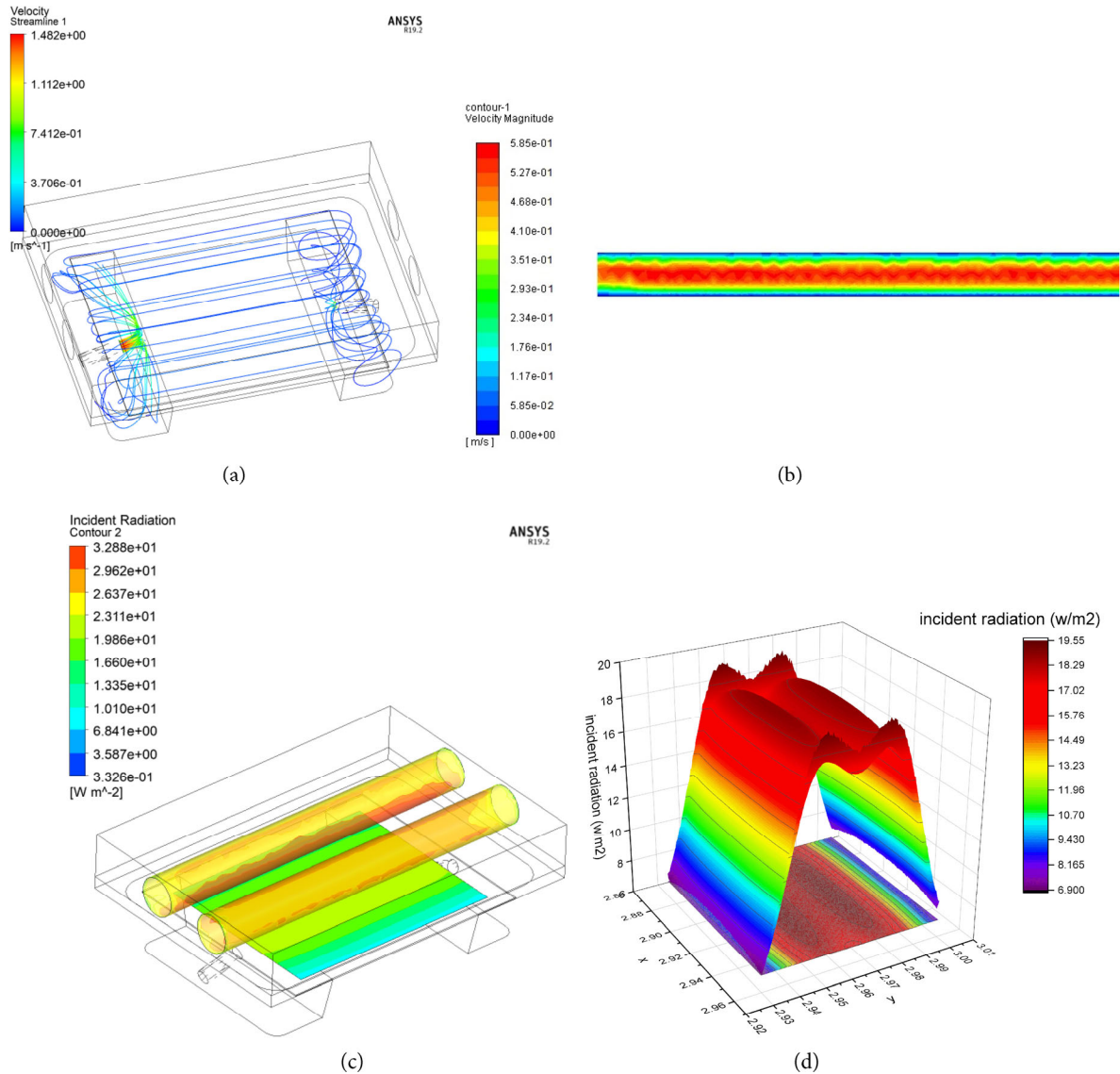
Fig. 11 (a) The predicted mixed air-VOC streamlines, (b) the predicted velocity field of the cross-sections of the reactor along the flow direction (c) the predicted irradiance field and (d) the predicted incident irradiance field at the catalyst surface

on the catalyst surface between two lamps. And the highest radiation intensity located at the lamp surface due to the superposition of both direct incident radiations from another lamp and reflected radiation from the catalyst.

Further implementing the kinetic reaction through UDF into the species transport equation of each control volume.

The flow field with PCO taking place was solved. Taking the operating condition #1 as an example, the VOC concentration fields at the plate and mid-plane were shown in Figure 12. Due to the uniform distributions of VOC in the reactor before lamps on, the VOC concentration field after the PCO reaction followed a similar pattern as the radiation
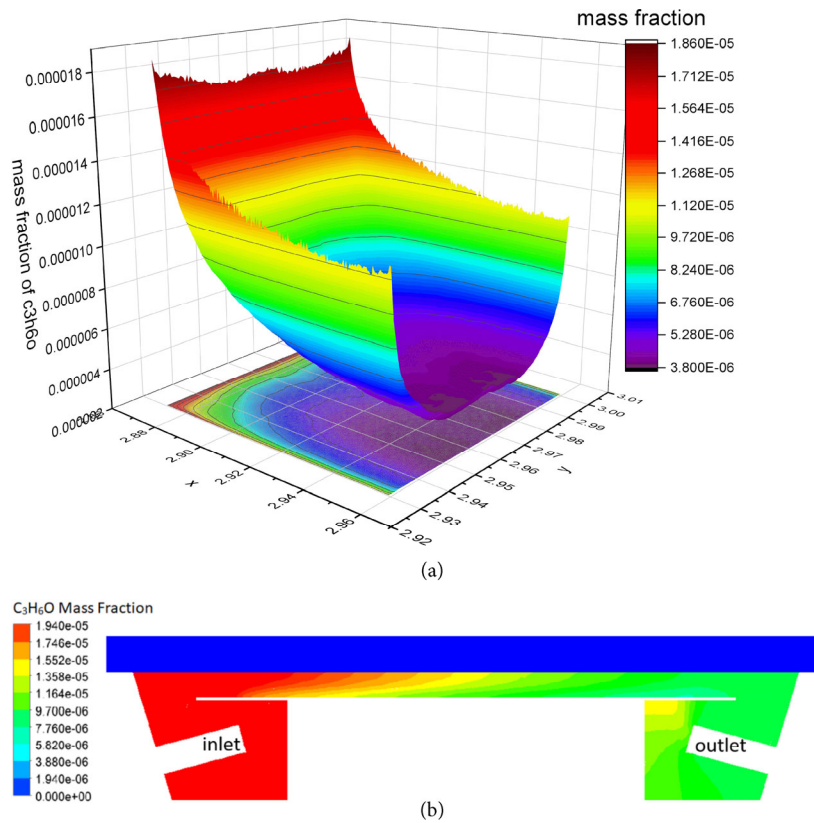
Fig. 12 The VOC concentration field at (a) catalyst surface and (b) mid-plane after turning on the UV-lamps

field. Moreover, VOC concentration decreased along the flow direction since both the UV-PCO reaction and the convection propagation were irreversible. From the mid-plane view of the VOC concentration field, the reaction occurred immediately after the VOC flow contacted the catalyst surface. With the effect of diffusion propagation, VOC molecules at the top part of the reactor moved down to catalyst surface and took reaction as well. Moreover, the left corner above the outlet had the VOC accumulation since the reactants hit the wall to create turbulence before ejecting from the outlet.

The predictions of overall VOC removal efficiency for the twelve operating conditions were tabulated in Table 4. It is noted the model predictions agreed well with the experimental data, although some deficiencies existed due to the residuals from the data fitting in the determination of model parameters. For the varying inlet VOC concentration, the increasing linear relationship between reaction rate r and inlet VOC concentration was observed from Eq. (24), while the removal efficiency decreased with the increase of inlet concentration (Table 4). With respect to the increase of air flow rate and relative humidity, both reaction rate and conversion efficiency decreased, which were the results of less contact time between VOC and catalyst and the competitive adsorption between VOC and water.

6 Model limitations and future work

The PCO mechanisms were quantitatively described by the light transport, mass transport and reaction models from the macroscopic to microscopic point of view. The reactor presented the non-ideal plug flow reactor characteristics (normalized σ^2 = 0.219 and negligible axial dispersion). However, the radial dispersion was assumed neglected whereas there was certain deficiency of the assumption (the radial velocity distribution see the Electronic Supplementary Material Figure S5) even though the model results were validatd by the experimental data. Thus, our future work is to develop a 2D mass transport model to account for the effects of the radial dispersion. Furthermore, the nature of the catalyst coating (macropores and mesopores) was revealed by the hierarchical mass transport model. However, the widely used 1D equations (considering PCO is a surface reaction at a no-thickness surface) were inadequate to represent the mass transport within the catalyst coating, i.e., along the coating thickness direction. Thus, another future work includes the development of an interrelated 3D light & mass transfer models within the porous media to account for the spatial effects of the light absorption and mass adsorption on the PCO reactions, and implementation of the meso &

Table 4 UV-PCO removal efficiency comparison by model and experimental data

No.	Inlet concentration (mg/m³)	Volume flow rate (L/min)	Water concentration (mg/m³)	UV-PCO removal efficiency		
				Experimental data	Model predictions	Difference
#1	23.99 ± 1.2		≈ 0 RH	0.523	0.521	0.38%
#2	47.98 ± 2.4	1± 0.006	≈ 0 RH	0.429	0.435	1.40%
#3	71.97 ± 3.6		≈ 0 RH	0.239	0.245	2.51%
#4	95.96 ± 4.8		≈ 0 RH	0.216	0.222	2.78%
#5		1 ± 0.006	≈ 0 RH	0.523	0.521	0.38%
#6	23.99 ± 1.2	2 ± 0.012	≈ 0 RH	0.309	0.312	0.97%
#7		3 ± 0.018	≈ 0 RH	0.245	0.287	17.14%
#8		4 ± 0.024	≈ 0 RH	0.141	0.139	1.42%
#9			3450 (15% ± 2%RH)	0.482	0.512	6.22%
#10	23.99 ± 1.2	1 ± 0.006	6900 (30% ± 2%RH)	0.293	0.296	1.02%
#11			11500 (50% ± 2%RH)	0.215	0.195	9.30%
#12			16110 (70% ± 2%RH)	0.121	0.115	4.96%

macroscopic co-simulation for a complete demonstration of the UV-PCO purification mechanism.

7 Conclusions

This paper has developed systematically numerical models to mathematically describe light transport, mass transfer and basic reaction mechanisms involved in heterogeneous PCO reaction within porous film coating. The light propagation and three-stage mass transfer have been developed and validated in consideration of light scattering, hierarchical mass transfer resistance (external boundary layer and macropore-mesopore) and local diffusion and adsorption. An element reaction kinetics model was successfully used here to explain correlations of adsorption, UV-PCO, competitive sites on the catalyst surface. After integrating with a CFD model for solving the mass, momentum and energy conservation, the transient and stable adsorption and UV-PCO processes as a function of time for indoor air purification were reproduced. The integration of the newly developed numerical models with CFD simulation shows the great potential of revealing the intrinsic complexity of UV-PCO on catalysts.

Acknowledgements

References

Adjimi S, Roux JC, Sergent N, Delpech F, Thivel PX, Pera-Titus M (2014). Photocatalytic oxidation of ethanol using paper-based nano-TiO₂ immobilized on porous silica: A modelling study. *Chemical Engineering Journal*, 251: 381–391.

Alberici RM, Jardim WF (1997). Photocatalytic destruction of VOCs in the gas-phase using titanium dioxide. *Applied Catalysis B: Environmental*, 14: 55–68.

ANSYS (2018). ANSYS Fluent Theory Guide. ANSYS Help System. ANSYS Academic Research.

Atkins P, de Paula J (2009). Atkins' Physical Chemistry, 8th edn. Oxford, UK: Oxford University Press.

Bielski BHJ, Cabelli DE, Arudi RL, Ross AB (1985). Reactivity of HO₂/O⁻₂ radicals in aqueous solution. *Journal of Physical and Chemical Reference Data*, 14: 1041–1100.

Boyjoo Y, Ang M, Pareek V (2014). Lamp emission and quartz sleeve modelling in slurry photocatalytic reactors. *Chemical Engineering Science*, 111: 34–40.

Bucholtz A (1995). Rayleigh-scattering calculations for the terrestrial atmosphere. *Applied Optics*, 34: 2733–2765.

Casado C, Marugán J, Timmers R, Muñoz M, van Grieken R (2017). Comprehensive multiphysics modeling of photocatalytic processes by computational fluid dynamics based on intrinsic kinetic parameters determined in a differential photoreactor. *Chemical Engineering Journal*, 310: 368–380.

Chawengkijwanich C, Hayata Y (2008). Performance of TIO₂ Powder Coated Packaging Film in Ethylene Removal. In: Proceedings of Europe-Asia Symposium on Quality Management in Postharvest Systems (Eurasia 2007), Bangkok, Thailand.

Cheng Y, Niu J, Du Z, Lei Y (2015). Investigation on the thermal comfort and energy efficiency of stratified air distribution systems. *Energy for Sustainable Development*, 28: 1–9.

Ciani A, Goss KU, Schwarzenbach RP (2005). Light penetration in soil and particulate minerals. *European Journal of Soil Science*, 56: 561–574.

Cuevas SA, Arancibia-Bulnes CA, Serrano B (2007). Radiation field in an annular photocatalytic reactor by the P1 approximation. *International Journal of Chemical Reactor Engineering*, 5(1). doi: https://doi.org/10.2202/1542-6580.1589.

Cussler EL, Cussler EL (2012) Fundamentals of Mass Transfer. Cambridge, UK: Cambridge University Press.

Denny F, Scott J, Pareek V, Gang DP, Amal R (2009). CFD modelling for a TiO_2-coated glass-bead photoreactor irradiated by optical fibres: Photocatalytic degradation of oxalic acid. *Chemical Engineering Science*, 64: 1695–1706.

Duran JE, Mohseni M, Taghipour F (2011). Computational fluid dynamics modeling of immobilized photocatalytic reactors for water treatment. *AIChE Journal*, 57: 1860–1872.

Džimbeg-Malčić V, Barbarić-Mikočević Ž, Itrić K (2012). Kubelka-Munk theory in describing optical properties of paper (I). *Tehnicki Vjesnik*, 19: 191–196.

Einaga H, Tokura J, Teraoka Y, Ito K (2015). Kinetic analysis of TiO_2-catalyzed heterogeneous photocatalytic oxidation of ethylene using computational fluid dynamics. *Chemical Engineering Journal*, 263: 325–335.

Elim HI, Cai B, Sugihara O, Kaino T, Adschiri T (2011). Rayleigh scattering study and particle density determination of a high refractive index TiO_2 nanohybrid polymer. *Physical Chemistry Chemical Physics*, 13: 4470.

Ishibashi K, Fujishima A, Watanabe T, Hashimoto K (2000). Quantum yields of active oxidative species formed on TiO_2 photocatalyst. *Journal of Photochemistry and Photobiology A: Chemistry*, 134: 139–142.

Ishii T, Ogawa T (2004). The coloring mechanism of boehmite-treated aluminum foil. *Journal of the Japan Society of Colour Material*, 77: 493–498.

Janecek M (2012). Reflectivity spectra for commonly used reflectors. *IEEE Transactions on Nuclear Science*, 59: 490–497.

Jarandehei A, de Visscher A (2009). Three-dimensional CFD model for a flat plate photocatalytic reactor: Degradation of TCE in a serpentine flow field. *AIChE Journal*, 55: 312–320.

Kast W (1985). Principles of adsorption and adsorption processes. *Chemical Engineering and Processing: Process Intensification*, 19: 118.

Kim SB, Hong SC (2002). Kinetic study for photocatalytic degradation of volatile organic compounds in air using thin film TiO_2 photocatalyst. *Applied Catalysis B: Environmental*, 35: 305–315.

Li Puma G, Salvadó-Estivill I, Obee TN, Hay SO (2009). Kinetics rate model of the photocatalytic oxidation of trichloroethylene in air over TiO_2 thin films. *Separation and Purification Technology*, 67: 226–232.

Luo H, Zhang C, Zhu J (2019a). Development of a numerical model for the hydrodynamics simulation of liquid-solid circulating fluidized beds. *Powder Technology*, 348: 93–104.

Luo H, Zhang G, Zhong L, Hashisho Z (2019b). Numerical simulation of a UV-PCO plate reactor. *IOP Conference Series: Materials Science and Engineering*, 609: 042011.

Malayeri M, Haghighat F, Lee CS (2019). Modeling of volatile organic compounds degradation by photocatalytic oxidation reactor in indoor air: A review. *Building and Environment*, 154: 309–323.

MATERION (n.d.). Reflectance in ThinFilms. Available at https://materion.com/-/media/files/advanced-materials-group/me/technicalpapers/reflectance-in-thin-films_all.pdf

Menter FR, Kuntz M, Langtry R (2003). Ten years of industrial experience with the SST turbulence model. In: Proceedings of the 4th International Symposium on Turbulence, Heat and Mass Transfer, Antalya, Turkey.

Muñoz-Batista MJ, Ballari MM, Kubacka A, Alfano OM, Fernández-García M (2019). Braiding kinetics and spectroscopy in photo-catalysis: the spectro-kinetic approach. *Chemical Society Reviews*, 48: 637–682.

Murakami S, Kato S, Ito K, Zhu Q (2003). Modeling and CFD prediction for diffusion and adsorption within room with various adsorption isotherms. *Indoor Air*, 13: 20–27.

Murakami Y, Endo K, Ohta I, Nosaka AY, Nosaka Y (2007). Can OH radicals diffuse from the UV-irradiated photocatalytic TiO_2 surfaces? Laser-induced-fluorescence study. *The Journal of Physical Chemistry C*, 111: 11339–11346.

Nosaka Y, Nosaka AY (2017). Generation and detection of reactive oxygen species in photocatalysis. *Chemical Reviews*, 117: 11302–11336.

Obee TN, Brown RT (1995). TiO_2 photocatalysis for indoor air applications: effects of humidity and trace contaminant levels on the oxidation rates of formaldehyde, toluene, and 1,3-butadiene. *Environmental Science & Technology*, 29: 1223–1231.

Pareek V, Chong S, Tadé M, Adesina AA (2008). Light intensity distribution in heterogenous photocatalytic reactors. *Asia-Pacific Journal of Chemical Engineering*, 3: 171–201.

Penndorf R (1957). Tables of the refractive index for standard air and the Rayleigh scattering coefficient for the spectral region between 0.2 and 20.0 μ and their application to atmospheric optics. *Journal of the Optical Society of America*, 47: 176–182.

Queffeulou A, Geron L, Schaer E (2010). Prediction of photocatalytic air purifier apparatus performances with a CFD approach using experimentally determined kinetic parameters. *Chemical Engineering Science*, 65: 5067–5074.

Salthammer T, Schulz N, Stolte R, Uhde E (2016). Human sensory response to acetone/air mixtures. *Indoor Air*, 26: 796–805.

Salvadó-Estivill I, Brucato A, Li Puma G (2007a). Two-dimensional modeling of a flat-plate photocatalytic reactor for oxidation of indoor air pollutants. *Industrial & Engineering Chemistry Research*, 46: 7489–7496.

Salvadó-Estivill I, Hargreaves DM, Li Puma G (2007b). Evaluation of the intrinsic photocatalytic oxidation kinetics of indoor air pollutants. *Environmental Science & Technology*, 41: 2028–2035.

Shehap AM, Akil DS (2016) Structural and optical properties of TiO_2 nanoparticles/PVA for different composites thin films. *International Journal of Nanoelectronics and Materials*, 9: 17–36.

Shinen MH, AlSaati SAA, Razooqi FZ (2018). Preparation of high transmittance TiO_2 thin films by Sol-gel technique as antireflection coating. *Journal of Physics: Conference Series*, 1032: 012018.

Snyder LR (1992). Theory of chromatography. *Journal of Chromatography Library*, 51: A1–A68.

Taghipour F, Mohseni M (2005). CFD simulation of UV photocatalytic reactors for air treatment. *AIChE Journal*, 51: 3039–3047.

Tobaldi DM, Lajaunie L, Rozman N, Caetano A, Labrincha JA (2019). Impact of the absolute rutile fraction on TiO$_2$ visible-light absorption and visible-light-promoted photocatalytic activity. *Journal of Photochemistry and Photobiology A: Chemistry*, 382: 111940.

Trujillo FJ, Safinski T, Adesina AA (2010). Oxidative photo-mineralization of dichloroacetic acid in an externally-irradiated rectangular bubble tank reactor: Computational fluid dynamics modeling and experimental verification studies. *Industrial & Engineering Chemistry Research*, 49: 6722–6734.

van Walsem J, Verbruggen SW, Modde B, Lenaerts S, Denys S (2016). CFD investigation of a multi-tube photocatalytic reactor in non-steady-state conditions. *Chemical Engineering Journal*, 304: 808–816.

Wang K, Tsai HH, Hsieh YH (1998). The kinetics of photocatalytic degradation of trichloroethylene in gas phase over TiO$_2$ supported on glass bead. *Applied Catalysis B: Environmental*, 17: 313–320.

Wang Z, Liu J, Dai Y, Dong W, Zhang S, Chen J (2012). CFD modeling of a UV-LED photocatalytic odor abatement process in a continuous reactor. *Journal of Hazardous Materials*, 215–216: 25–31.

Yu K-P, Lee GWM, Huang W-M, Wu C, Yang S (2006). The correlation between photocatalytic oxidation performance and chemical/physical properties of indoor volatile organic compounds. *Atmospheric Environment*, 40: 375–385.

Yu H, Zhang K, Rossi C (2007). Experimental study of the photocatalytic degradation of formaldehyde in indoor air using a nano-particulate titanium dioxide photocatalyst. *Indoor and Built Environment*, 16: 529–537.

Zhang L-Z (2013). Conjugate heat and mass transfer in adsorbent ducts. In: Conjugate Heat and Mass Transfer in Heat Mass Exchanger Ducts. Waltham, MA, USA: Academic Press.

Zhang G, Wang H, Guo S, Wang J, Liu J (2016). Synthesis of Cu/TiO$_2$/organo-attapulgite fiber nanocomposite and its photocatalytic activity for degradation of acetone in air. *Applied Surface Science*, 362: 257–264.

Zhang G, Peyravi A, Hashisho Z, Sun Z, Liu Y, Zheng S, Zhong L (2020). Integrated adsorption and photocatalytic degradation of VOCs using a TiO$_2$/diatomite composite: effects of relative humidity and reaction atmosphere. *Catalysis Science & Technology*, 10: 2378–2388.

Zhong L, Haghighat F (2011). Modeling and validation of a photocatalytic oxidation reactor for indoor environment applications. *Chemical Engineering Science*, 66: 5945–5954.

Zhong L, Haghighat F, Lee CS (2013). Ultraviolet photocatalytic oxidation for indoor environment applications: Experimental validation of the model. *Building and Environment*, 62: 155–166.

Zhu X, Chang D, Li X, Sun Z, Deng X, Zhu A (2015). Inherent rate constants and humidity impact factors of anatase TiO$_2$ film in photocatalytic removal of formaldehyde from air. *Chemical Engineering Journal*, 279: 897–903.